OPEN ACCESS
IOP Publishing
Superconductor Science and Technology
Supercond. Sci. Technol. **37** (2024) 095013 (16pp)
https://doi.org/10.1088/1361-6668/ad6a9c

Investigating the effect of rolling deformation on the electro-mechanical limits of Nb_3Sn wires produced by RRP® and PIT technologies

T Bagni[1,2,*], C Calzolaio[3], G Bovone[1], J Ferradas-Troitino[4], C Barth[4], A Ballarino[4] and C Senatore[1,5]

[1] Department of Quantum Matter Physics, University of Geneva, Geneva, Switzerland
[2] Department of Physics and Astronomy, Uppsala University, Uppsala, Sweden
[3] Department of Accelerator Technology, Paul Scherrer Institute, Villigen, Switzerland
[4] European Organization for Nuclear Research CERN, Geneva, Switzerland
[5] Department of Nuclear and Particle Physics, University of Geneva, Geneva, Switzerland

E-mail: Tommaso.bagni@physics.uu.se

Received 5 December 2023, revised 24 July 2024
Accepted for publication 2 August 2024
Published 12 August 2024

Abstract

Future high-field magnets for particle accelerators hinge on the crucial development of advanced Nb_3Sn wires engineered to withstand the large stresses generated during magnet assembly and operation. The superconducting properties of Nb_3Sn enable the design of compact accelerator-quality magnets above 10 T, but at the same time the brittleness and strain sensitivity of the material impose careful consideration of the mechanical limits. In addition, accelerator magnets are wound using Rutherford cables and the cabling process generates deformations in the wire that can affect its electro-mechanical performance. This paper reports on the impact of the rolling deformation on the transverse stress tolerance of high-performance restacked-rod-process (RRP®) and powder-in-tube (PIT) Nb_3Sn wires. Rolling deformation was used to mimic the effect of cabling on the wire shape. Deformed samples were compared to reference round wires in term of stress dependence and irreversible limit (σ_{irr}) of the critical current (I_c) under transverse compressive loads up to 240 MPa. Experiments were performed at 4.2 K, 19 T, on resin-impregnated single wires that imitate the operating conditions in a Rutherford cable of an accelerator magnet. The results show that rolling deformation has a detrimental effect on the initial I_c of PIT wires, but it does not influence the behavior of the wire under stresses above 70 MPa. On the other hand, the deformation of RRP® wires leads to an improved σ_{irr} without affecting the initial I_c. Additionally, a 2D-mechanical finite element method model of the RRP® wire was developed to investigate the impact of the wire geometry on the plastic deformation of the copper matrix, which induces residual stresses on Nb_3Sn and is the main cause for the permanent reduction of I_c. Based on the model results, an alternative layout of the wire was proposed that improves its stress tolerance without affecting its electrical transport properties.

* Author to whom any correspondence should be addressed.

Original content from this work may be used under the terms of the Creative Commons Attribution 4.0 licence. Any further distribution of this work must maintain attribution to the author(s) and the title of the work, journal citation and DOI.

© 2024 The Author(s). Published by IOP Publishing Ltd

Keywords: Nb3Sn, electromechanical properties, critical current degradation, irreversible stress limit, electromechanical model, accelerator magnets

1. Introduction

The maximum energy that a circular accelerator can reach in is proportional to the radius of the accelerator and to the magnetic field generated by its bending dipoles [1]. As a result, the discoveries achieved in High Energy Physics are strictly related to the advancements in the technology of high-field superconducting magnets. Nowadays, the development of next generation superconducting magnets for accelerators is mainly driven by the need of producing fields beyond those of the magnets of the large hadron collider (LHC). This includes the magnets developed for the high-luminosity upgrade of LHC (HL-LHC), which is currently under construction at CERN [2], and the preliminary studies for the future circular collider (FCC) [3]. The goal of HL-LHC is to increase the integrated luminosity, which measures the collected data size of a particle collider and is thus an indicator of its performance, by a factor of ten. Key technology for achieving this goal is the Nb_3Sn used in the quadrupole magnets of the HL-LHC interaction regions at Point 1 and Point 5. These magnets reach a peak field in the coils in the range of 12 T. On the other hand, FCC aims to achieve a dipole field level of 16 T, needed to reach a proton–proton collision energy of 100 TeV at the center of mass, in a 100 km circular tunnel.

Nb_3Sn is the superconducting material chosen for the HL-LHC quadrupole magnets and is also a candidate for the FCC-hh [3]. This material has a upper critical field close to 30 T at 4.2 K [4] and a critical temperature of about 18 K [5]. It was discovered in the 60 s, but due to its brittleness and complicated production methods, it took decades to achieve its industrial maturity, including 20 years of research and development to build the toroidal coils and central solenoid of the ITER fusion reactor [6]. Because of the brittle nature of Nb_3Sn, the manufacturing of magnets with this superconductor follows the 'wind and react' technique. For accelerator magnets, this consists in winding a magnet coil with Rutherford cables, typically glass-fiber insulated, made of multi-filamentary wires. Each wire contains the Nb and Sn precursors cased in a high-purity Cu matrix. In this form the Nb_3Sn wires are assembled into Rutherford cables, which are later wound into coils. During this process, distortion and plastic deformation are induced in the wires. The cabling deformations can result in a reduction of critical current (I_c) and Cu purity in the final conductor after reaction [7, 8]. After the winding, the coil undergoes the heat treatment (HT), with a peak temperature normally around 650 °C–670 °C. During the HT the precursors react forming the superconducting Nb_3Sn phase. At this stage, the coil becomes fragile, and undergoes a resin impregnation process which fills the interstitial spaces with a polymer, thus providing cohesion and support to the brittle Nb_3Sn wires. The finished coil is still stress and strain sensitive, and a careful evaluation of its mechanical limits is needed to achieve the field required during operation.

Recent studies performed on different possible designs of the 16 T dipoles for the FCC-hh, namely, cosine–theta [9], block-coil [10], common-coil [11] and canted cosine–theta [12], highlighted the large mechanical loads that would be generated in these magnets. According to the models, the electromagnetic forces would determine peak stresses on the Nb_3Sn conductor in the 150–200 MPa range at the operation field [13]. On the other hand, a study on the effect of pre-stress on Nb_3Sn Rutherford cables [14] showed that nominal transverse stresses applied at room temperature begin to cause permanent degradation in critical current between 150 and 175 MPa, proving the profound impact of stress on magnet design. Additional studies on the onset and evolution of mechanical damage in Rutherford cables have shown that micro-cracks may be induced in the Nb_3Sn wires before I_c degradation is detected [15]. In dipoles magnets, the peak stress on the conductor is typically localized in the midplane and oriented in the transverse direction of the Rutherford cable, and such a stress induces a large decrease of I_c [16, 17]. This decrease has two distinct components: the reversible one, which is fully recovered by removing the external load [18]; and the irreversible one, which occurs when the I_c reduction becomes permanent. The irreversible reduction of the transport properties can be generated by residual stresses on the Nb_3Sn crystal lattice, caused by the plastic deformation of the Cu matrix, as well as by the formation of cracks in the brittle Nb_3Sn filaments. Studies pointed to filaments breakage as the main cause for the I_c permanent reduction [19]. Recent results indicate that also the residual stresses, and the consequent upper critical field, B_{c2}, decrease, are responsible for the I_c drop in restacked-rod-process (RRP) and powder-in-tube (PIT) wires [20–22]. The role of the B_{c2} reduction in I_c degradation of RRP® and PIT wires can be analytically evaluated fitting the $I_c(B)$ results as presented in [22].

The results of an electromechanical test campaign, carried out in the framework of the European project EuroCirCol, have proven that it is possible to extract quantitative information about the degradation of a Rutherford cable from the measurement of a single wire under transverse stress [23]. The study was carried out on the PIT Nb_3Sn wire developed for the FRESCA-2 dipole [24]. It was performed exploiting a modified Walter spring (WASP), also called Compressive WASP or C-WASP, developed at the University of Geneva (CH) [25]. The probe makes it possible to test the critical current of resin-impregnated single wires at 4.2 K in magnetic fields ranging between 16 and 19 T, while exerting a transverse stress up to

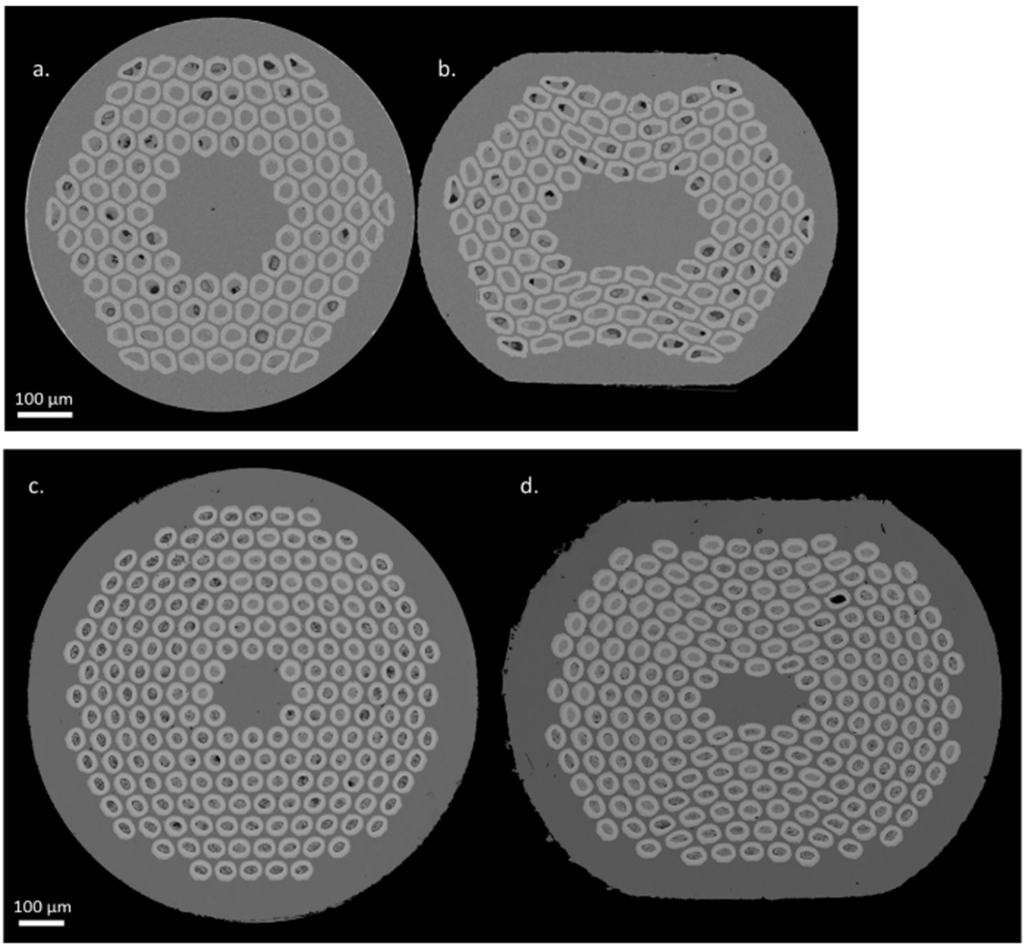

Figure 1. Cross sections of round (a) and rolled (b) 108/127 RRP® wires and round (c) and rolled (d) PIT 192 after the reaction heat treatment. The diameters of the wires before rolling are 0.7 mm and 1.0 mm, respectively.

∼240 MPa. A similar analysis was also performed on RRP® Nb_3Sn wires, designed for the HL-LHC MQXF quadrupole [19] and 11 T dipole [22] magnets to study the tolerance to transverse stress of this wire technology.

In the cited tests on a single wire [19, 22], and [23], the measurements were performed on round wires. On the other hand, during the production of Rutherford cables, wires are deformed, and it is therefore necessary to evaluate carefully what is the influence of such a deformation on the electromechanical behavior of the wire and, consequently, on the stress tolerance of the cable.

The primary objective of this study is to assess the impact of the cabling deformation on high-performance PIT and RRP® Nb_3Sn wires. Round wires have been passed through a rolling mill prior to the reaction HT to create what we refer to as 'rolled wires', as shown in figure 1, in order to reproduce a wire deformation representative of what occurs during the production of cables. A 15% reduction in wire diameter in the rolling direction was chosen because it produces an effect on I_c and residual-resistivity-ratio comparable to that caused by cabling in a Rutherford configuration [26]. Following the same preparation and measurement procedures as for their round counterparts, the rolled wires were then subjected to the same HT and tested using the C-WASP probe. Finally, a comparative analysis of stress dependence and irreversible limit (σ_{irr}) of I_c was performed. Where the σ_{irr} is arbitrarily defined as the stress corresponding to 5% of I_c degradation.

The second objective of the paper is to investigate numerically how the wire geometry, i.e. round vs. rolled, influences the stress redistribution within the wire under transverse load and, thus, affects the Cu plastic deformation and the residual stresses on Nb_3Sn, which leads to the permanent reduction of I_c. As a result, we built a 2D mechanical finite element method (FEM) model to study these phenomena in COMSOL Multiphysics®. FEM was used to analyze how the plastic deformation of the Cu matrix is distributed in relation to the wire geometry, and the location of the residual stresses, comparing round and rolled wires. The model was designed on RRP® wires since they do not exhibit any degradation in I_c due to the 15% rolling process, while PIT wires degrades upon rolling. The model geometries were extracted from the scanning electron microscope (SEM) images of the wires cross section using an image analysis algorithm based on machine learning [27, 28], and then imported in COMSOL Multiphysics®.

Finally, using the information obtained from the model, we simulated the properties of an RRP® wire with an alternative sub-element layout conceived to obtain conductors that are

more stress-resistant. In such a wire, the superconducting sub-elements are distributed in order to minimize the effect of the Cu plasticization leading to an increase of σ_{irr} without affecting the electrical transport properties.

The paper begins with the description of the experimental setup and the wires information before moving to the discussion of the measurements results. The following sections describe the mechanical FE model and present the comparison between round and rolled wire. The final section is dedicated to the simulation of the properties of the new wire design expected to be more stress-resilient and it is followed by the conclusions.

2. Experimental details

2.1. Samples characteristics

In this study, two Nb_3Sn wires are analyzed; table 1 lists the key details of both wires, including the reaction HT schedules. The first sample, #31712, is a PIT wire developed for the FRESCA-2 dipole [24]; it has 192 filaments, a Cu/non-Cu volume ratio of about 1.22 and a diameter of 1.0 mm before the rolling deformation. The round version of the same wire was tested in [23]. The second sample, #073A02, is an RRP® wire developed for the 11 T dipole program of HL-LHC, and has a diameter of 0.7 mm before rolling. The wire has 108 Nb_3Sn sub-elements which follow the hexagonal 108/127 disposition with a Cu/non-Cu ratio of about 1.2. The electromechanical characterization of the round version of this RRP® wire is reported in [22]. Both wire types were rolled at CERN applying a 15% transversal deformation.

2.2. Transverse measurement setup

The C-WASP probe used for the critical current under transverse stress measurements has a geometry similar to a WASP and the sample holder is made of two parts. The lower part consists in a **U**-shaped groove, designed to contain the wire and its impregnation, the width of the groove being adapted to the wire diameter. The upper section has an anvil that fits into the groove and presses against the impregnated wire. The upper part is fixed whereas the lower part can move axially transmitting the transverse force to the impregnated wire. The gauge length is 126 mm, which is multiple times longer than the wires twist pitch, allowing to apply an electric field criterion of 0.1 μV cm^{-1} for the determination of I_c. During the mounting of the rolled sample, the flat face of the wire is oriented in order to face the C-WASP anvil. The orientation of the sample is a crucial aspect for this test. In the case of the measurement on a round wire, because of its symmetry, there is no effect due to the sample rotation along the axial direction. On the other hand, when measuring a rolled wire, its orientation in the groove plays a role on the outcome of the measurement. As mentioned in the introduction, the analyzed Nb_3Sn wires follows the 'wind and react' process, i.e. the wire sample is shaped in a helical form prior the HT to fit then into the C-WASP. Therefore, the wire is mounted on a stainless-steel reaction mandrel that follows the C-WASP geometry in such a way that, after the HT, one of the flat surfaces will face the anvil when placed on the compressive WASP. However, in this phase, the wire is free to move and/or rotate in the reaction mandrel due to thermal expansions and contractions, and thus it is not possible to control the final sample orientation. Typically, each HT batch consists of 6–8 samples. Following the HT, a visual inspection is conducted to select the reacted samples with the most uniform orientation, specifically those where the flat surfaces closely align with the C-WASP anvil. These selected samples are then transferred to the C-WASP for the measurement. It should be noted that the orientation can change along the wire length adding a degree of difficulty in selecting the samples most adequate for the measurement. A simplified schematic of the C-WASP setup is shown in figure 2.

The current is injected in the sample by soldering the wire onto the copper terminals of the C-WASP. The sample impregnation is carried out with a de-gassed epoxy-resin type-L mixture provided by R&G Fasefrverbundwerkstoffe GmbH. This type of impregnation has a similar elastic modulus compared to the CDT-101 K resin, which is used for the impregnation of HL-LHC Nb_3Sn coils, but it has easier handling because no HT is required during the cure [29, 30]. For more information on the C-WASP setup, please refer to [19, 23, 31] and [32]. The maximum applied transverse force is 35 kN and the corresponding stress is calculated by dividing the applied force by the groove dimensions, which are 126 mm in length and 1.0 mm or 1.15 mm in width, depending on the wire diameter, in this case the 0.7 mm RRP® and the 1.0 mm PIT, respectively. The depth of the groove once the anvil is in contact with the epoxy can slightly vary due to the closing procedure, but it is about 1.5 mm. The force is increased in 1 kN steps and the I_c under load (I_c^{load})is measured after each increment. Moreover, after every other step, the force is removed and the I_c after unload (I_c^{unload}) is measured. By convention, the irreversible stress limit σ_{irr} is reached when I_c^{unload} decreases to 95% of the initial critical current, I_{c0}. At the end of the measurement campaign, the sample is dismounted. During this destructive operation, the impregnation homogeneity is evaluated; in cases of the presence of bubbles in the epoxy or non-impregnated regions, the measurement is considered 'failed' and repeated on a new sample. When the tests result in the same irreversible limit on at least two different samples without noticing any deviation from the ordinary during the destructive unmounting of the sample, we consider the wire successfully measured. Only the results from one of the successful measurements per each wire are shown here for the sake of clarity. Since during our measurement campaign it was found that the irreversible limit of the rolled wires is lowered if the flat face of the sample is not aligned with the anvil, repeating the measurement also helps with the detection of any possible misalignment.

3. Results and discussions

3.1. #31712—PIT 192

Two rolled samples of the PIT wire from the billet #31712 were tested under transverse load in the C-WASP setup using

Table 1. Main characteristics of the investigated Nb_3Sn wires.

Billet ID	Wire design	Diameter (before deformation)	Width after deformation	I_c (16 T) (A) I_c (19 T) (A)	Heat treatment	C-WASP groove width (mm)
#31712	PIT 192%–15% rolled	1.0 mm	∼1.09 mm	337 164	620 °C/100 h + 640 °C/90 h	1.15
#073A02	RRP® 108/127%–15% rolled	0.7 mm	∼0.76 mm	185 67	210 °C/48 h + 400 °C/48 h + 650 °C/50 h	1.00

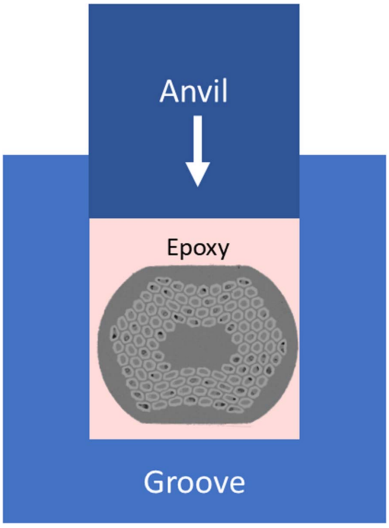

Figure 2. Working schematic of the C-WASP setup with a rolled wire sample. The wire is inserted in the groove and impregnated with epoxy. The stress is exerted through the anvil in contact with the epoxy. In case of rolled wire, the flat surface is positioned parallel to the anvil face.

a groove width of 1.15 mm. The two examined samples present similar initial I_c and irreversible limit, therefore for simplicity only one set of data is depicted here. In figure 3, the rolled wire is compared to the round sample measured in [23], both wires having been tested in the C-WASP at 4.2 K and 19 T. The plot (a) displays the dependence of I_c from the applied transverse stress, while in plot (b), the same dependence is shown normalizing I_c to the initial critical current, I_{c0} of each sample. In both plots the full symbols represent measurements taken while the force was applied, whereas the open symbols represent data acquired after the force was released.

Plot (a) shows a difference in the initial I_c between the round wire and the rolled one, of about 15 A, which corresponds to about 9% of the initial current of the round wire. This diminution caused by the 15%-rolling deformation is peculiar of the Nb_3Sn PIT technology. In the production of Nb_3Sn wires via the PIT method, Nb-alloy tubes filled with Sn and $NbSn_2$ powders are used as the wire sub-element. Many of these tubes are then incorporated into a Cu matrix, forming the wire. During HT, Sn diffuses from the inner to the outer wall of the Nb-alloy tubes. The outer wall of the tube acts as a diffusion barrier that maintains the Cu matrix purity. When the tubes are assembled and drawn down to the final wire diameter, the deformation affects the tube geometry, especially at the center of the wire, where they become highly anisotropic [7, 8]. Early-stage radial Sn diffusion to the tube outer wall can cause Sn leaks into the Cu matrix, disrupting Nb_3Sn phase formation and diminishing the wire I_c [33]. This effect plays a major role in the observed discrepancies in electric transport capacity between round and rolled wire samples, as shown in figure 3.

On the other hand, round and rolled wires exhibit very close I_c^{load} values starting from 70 MPa, see figure 3(a). This may be due to two phenomena interacting with each other. First, as said, the filaments at the center of the wire are those more affected by the rolling deformation. Second, the filaments most affected by the transverse load applied during the test are also located in the center of the wire [31]. Previous studies have shown that the permanent decrease of I_c in round wires is caused by residual stresses of the Nb_3Sn lattice due to the plastic deformation of the copper matrix [21, 22]. Combining these notions, we may infer that plasticization of round and rolled wires begins in the regions where stress levels are the highest, which are at the center of the wire. This assumption is reinforced by the findings of our RRP® wire modeling (see Section 5), which indicate that peak stresses accumulate at the wire core. As a result, the reduction of current-carrying properties begins in the area at the center of the wire and spreads outward as the applied load increases. In the case of the rolled wire, the internal filaments have a limited contribution to the overall I_c; thus, initially, the load does not have a detrimental effect on the wire performance. However, once stress levels

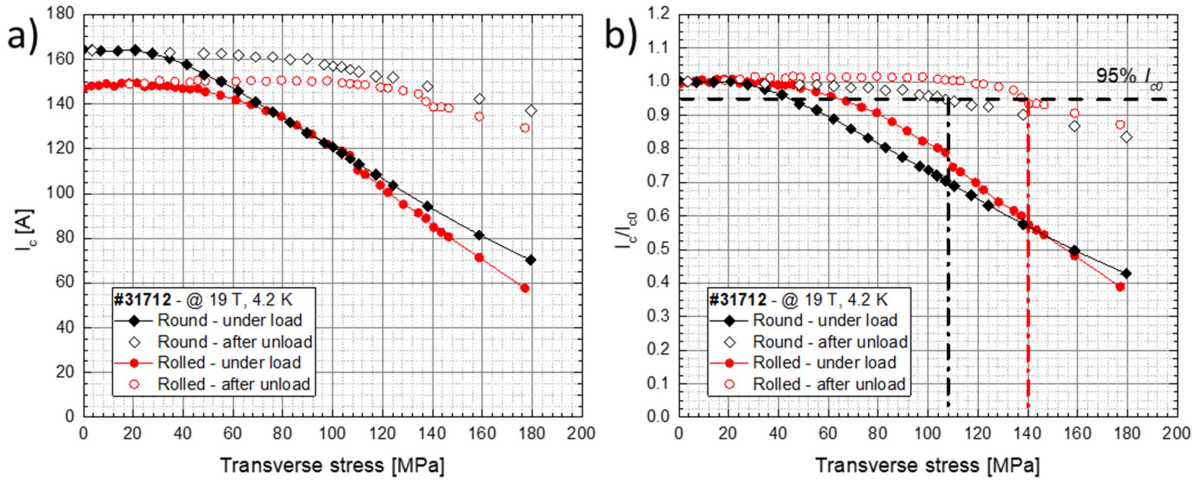

Figure 3. (a) Dependence of I_c on the applied transverse stress for the 1.0 mm PIT wire round (black diamond) and 15% rolled (red circles). (b) Dependence on the applied transverse stress of I_c normalized to the corresponding I_{c0} for each of the two PIT wires. Solid and open symbols correspond to the measurement under load and after unload, respectively. The vertical dashed lines in (b) indicate the irreversible stress limits.

surpass 60 MPa, the filaments less deformed by rolling start to be affected, and the current reduction evolves similarly to what observed in round wires. In addition, the difference in I_c^{unload} between rolled and round wires is reduced and ranges between 3% and 6% above 100 MPa. Overall, the two wires behave very similarly both under load and after unload above 100 MPa.

When comparing the values of I_c/I_{c0}, which are illustrated in figure 3(b), the rolled wire has an apparently higher σ_{irr}, 140 MPa, than the round wire, whose σ_{irr} is only 110 MPa. However, this is only a consequence of the definition of σ_{irr}, which is linked to the value of I_{c0}. Furthermore, the decrease of I_c^{unload}, i.e the irreversible reduction of I_c due to the transverse stress, starts at about 50 MPa in the round sample, while the effect on the rolled wire begins at higher stresses, exceeding 100 MPa. These results reflect the combined effect of the rolling, which reduces I_{c0}, and the stress accumulation in the wire core. Therefore, the permanent decrease of I_c becomes evident only at higher stresses when the plasticization reaches more external filaments. In conclusion, the gain in σ_{irr} provided by the wire deformation is only illusory, and, under load, the rolled wire behaves similarly to the round one, therefore the rolling process reduces the wire I_{c0} but it is not detrimental on the electromechanical behavior of PIT wires under loads exceeding 100 MPa.

3.2. #073A02—RRP® 108/127

Two rolled samples of the RRP® wire from the billet #073A02 were tested under transverse stress in the C-WASP setup using a groove width of 1.0 mm. The two measured samples present similar initial I_c and irreversible limit, therefore for simplicity only one set of data is depicted here. In figure 4, the rolled wire is compared to the round sample examined in [22], both wires having been tested in the same C-WASP at 4.2 K and 19 T. The plot (a) displays I_c as function of the applied transverse stress, while in plot (b), the same dependence is shown with I_c normalized to the corresponding I_{c0} of each sample. In the plots, full symbols represent the results while the force was applied, whereas open symbols represent the measurements acquired after the force was released.

Differently from the PIT wire in section 3.1, this RRP® wire does not experience a substantial reduction of I_{c0} as a result of the rolling process. On the contrary, the rolled wire exhibits a value of I_{c0} that is ∼4% higher compared to the round wire. The absence of rolling degradation is consistent with what reported in [7], where it was shown that rolling deformations below 30% are not affecting I_c in RRP® wires. On the other hand, the increase of I_c due to rolling process is rather unusual. We argue that this variation is not intrinsic to the rolling deformation. It could be ascribed to the I_c variability along the wire length within the same billet, as well as to our experimental condition. A thorough examination of round RRP® wires using the C-WASP setup in [19] revealed that the initial axial strain condition has an impact on the wire electromechanical response under transverse stress. In other words, the tension applied on the sample while being mounted on the C-WASP can have an impact on the wire strain state and, consequently, on the initial critical current. In particular, a difference in the initial strain as small as 0.02%, equivalent to 10 N of applied pulling force during the mounting, is sufficient to lead to the observed increase by 4% of I_{c0} [19].

The normalization of I_c to I_{c0}, shown in figure 4(b), compensate the difference in the initial current. Once normalized, the two samples, round and rolled, behave very similarly under load. On the other hand, the σ_{irr} of the rolled wire is higher compared to that of the round sample, the values being ∼185 MPa and ∼160 MPa, respectively. Therefore, we can conclude that for this type of RRP® wire, the rolling

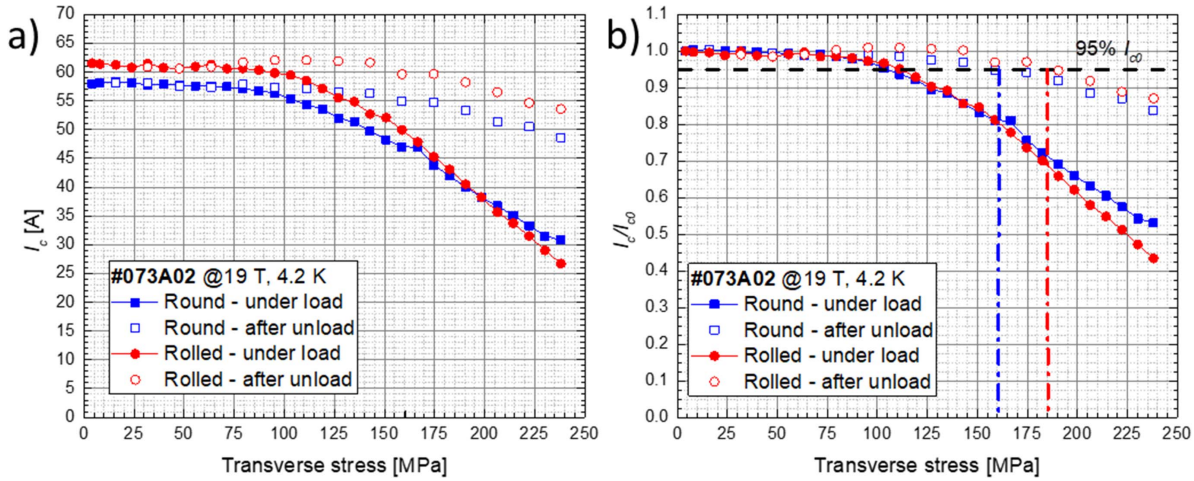

Figure 4. (a) Dependence of I_c on the applied transverse stress for the 0.7 mm RRP® wire round and rolled. (b) Dependence on the applied transverse stress of I_c normalized to the corresponding I_{c0} for each of the two wires. Solid and open symbols correspond to the measurement under load and after unload, respectively. Dashed lines indicate the irreversible stress limits.

deformation not only is not detrimental but even results in an increase of the irreversible limit of about 15%. This observation implies that in the case of rolled wire, the intuitive notion that applying pressure to a flat surface results in a broader and less concentrated distribution of stress is accurate, as will be proven by the following FEM analysis.

4. Model description

The FEM model used in this study is based on [31]. The aim of the simulation is to visualize the stress/strain distribution in the RRP® wire cross section under the conditions of our experiment. The model considers the elastoplastic behavior of the various materials presents in the wire cross-section, and allows for the calculation of the critical current density from the strain distribution. Both round and rolled configurations were analyzed using this FEM tool. A 2D plain strain approach was used in the simulations. Plane strain refers to a state of strain that causes deformation in one or two dimensions but not in the third one. In our case the material is free to deform in two directions, X and Y, but it is constrained in the third dimension, i.e. the wire length, thus the longitudinal strain in the Z-dimension is assumed to be zero. The C-WASP samples are single wires partially blocked at the ends with a length much larger than the cross-section diameter (126 mm: 0.7 mm). In this case, we consider the plain strain approximation to be sufficient to capture the general behavior of the wires. The wire geometry used in the model has been extracted from a SEM image of the RRP® wire cross section using the tomography analysis tool developed in [28]. As the main goal of the simulation is to study the difference between round and rolled wires, we selected two cross sections with similar orientation of the sub-elements to be used to construct the model geometry, see figure 1.

The wire cross section is composed by three domains: the copper (Cu) matrix, the Nb_3Sn sub-elements, and the α-bronze in the sub-element core. The Nb_3Sn and the bronze are formed during the wire HT [34]. In addition, to simulate the C-WASP measurement, the wire was surrounded by epoxy during the load/unload phase, as showed in figure 5. The materials characteristics used in the model are summarized in table 2 and collected from a standard strain–stress measurement performed at the University of Geneva [35] on the investigated RRP® wire at cryogenic temperature. The cool down of the wire is not considered in the model. The load was applied on the top of the epoxy as a distributed total force, see red arrows in figure 5. During the C-WASP measurements, the deformation of the anvil is negligible, so the connection between the anvil and the epoxy (wall number 1) was modeled as a rigid connector that made it possible to prescribe zero displacements and rotations. Also, the deformation of the groove was negligible, and a zero prescribed displacement along the x direction was imposed for walls 2 and 4. Finally, zero displacements were imposed along both the x and y directions, as well as zero rotations, to wall number 3.

The formation of Kirkendall voids inside the Nb_3Sn sub-elements during the HT [27, 36, 37] and their detrimental effect on the mechanical limits of the wires is well known [38]. However, in this study, the presence of Kirkendall voids was neglected for two reasons. Firstly, the voids in RRP® wires are not homogenously distributed and they show a large variation in sizes and shape. They typically have a length of several hundred micrometers and, at their widest point, can almost entirely fill the sub-element [21, 27]. Due to this significant variability, selecting a particular voids distribution in a 2D cross section would bias the mechanical simulation result when determining the I_c reduction based on the strain distribution. Secondly, the main objective of the FEM is to provide a picture of the plastic strain distribution in relation to the wire geometry. Therefore,

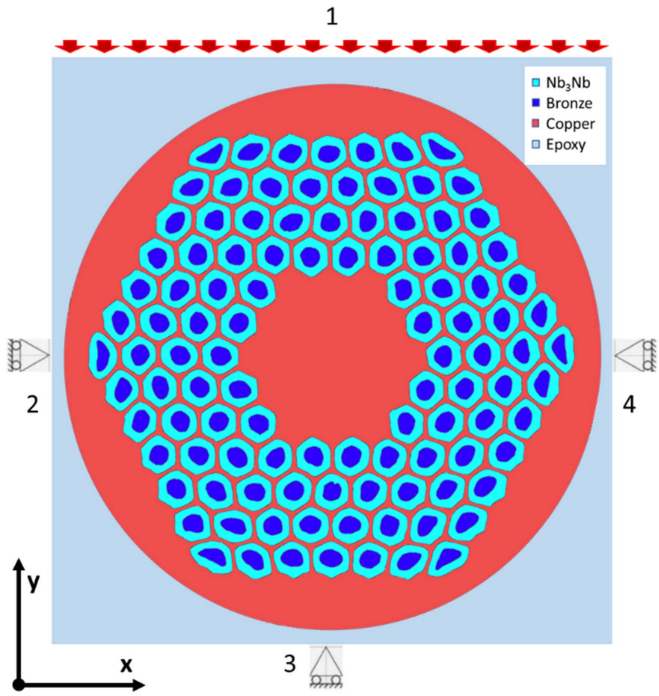

Figure 5. The round wire model geometry used in the FEM. The wire domains are shown in different colors: copper matrix in red, Nb_3Sn sub-elements in cyan and bronze cores in blue. The wire is surrounded by epoxy. The red arrows show the surface on which the load is applied.

Table 2. Mechanical properties corresponding to the materials used in the model, property data collected from [31] and [39].

Material	E (GPa)	Poisson's ratio	Behavior	Yield stress (MPa)
Nb_3Sn	80	0.36	Elastic	—
Copper	137	0.35	Elastoplastic	86.2
Bronze	142	0.35	Elastoplastic	119
Epoxy	8	0.3	Elastic	—

to a first approximation, voids can be neglected. The effect of the voids in the wire as well as the 3D geometry reconstruction should be considered in a quantitative simulation for this type of wire.

The equilibrium equation is given by Newton's second law. For the material frame formulation used in COMSOL Multiphysics, a Lagrangian version of the equation is used:

$$\rho_0 \frac{\partial^2 u}{\partial t^2} = 0 = \nabla \cdot (FS)^T + F_V \tag{1}$$

F_V is a body force, F is the deformation gradient and FS is the first Piola Kirchhoff stress. This equation is solved using the principle of virtual work. The key element of the simulation, beside the wire geometry, is to consider the elastoplastic deformation. When the material deforms plastically, its mechanical properties change. This manifests itself as a change in the geometry and position of the yield surface (commonly referred to as the loading surface). The evolution of the initial yield surface during plastic deformation is governed by the work-hardening rule. A yield criterion is necessary to define the stress condition under which plastic deformation occurs. The yield surface can be described as $F_y = f(\sigma) - \sigma_{ys}$, where σ_{ys} is the yield stress and the scalar function $f(\sigma)$ is called effective stress.

The evolution of the plastic deformation, referred as plastic flow, defines the increment of the plastic strain tensor and the current state of stress and it is defined by:

$$\dot{\varepsilon}_p = \lambda \frac{\partial Q_p}{\partial \sigma} \tag{2}$$

where λ is called plastic multiplier and Q_p is the plastic potential. In this model, the plastic potential and the yield surface coincide with each other (associated flow rule). The yield surface encloses the elastic region defined by $Fy < 0$. The plastic flow occurs when $Fy = 0$.

The model assumes the von Mises stress as the yield criterion, such that $f(\sigma) = \sqrt{3 \cdot J_2(\sigma)}$, and $f_y = \sqrt{3 \cdot J_2} - \sigma_{ys}$. Where $J_2(\sigma)$ is the second invariant of the deviatoric stress.

An isotropic hardening rule [40] describes the plastic history dependent yield criterion [31, 39]. The hardening function, σ_h, is the stress added to the initial yield stress as a

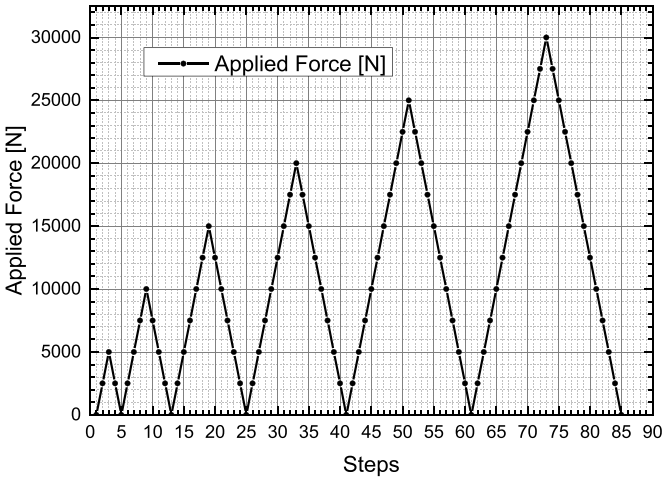

Figure 6. Load/unload loop applied during the simulation, the applied force as function of the iteration steps is depicted.

function of the equivalent plastic strain, see equation (3). The choice of isotropic hardening function may affect the results for the cyclic loads.

$$\sigma_{\mathrm{h}}\left(\varepsilon_{\mathrm{pe}}\right)=\sigma_{\mathrm{ys}}\left(\varepsilon_{\mathrm{total}}\right)-\sigma_{\mathrm{ys0}}. \tag{3}$$

$\sigma_{\mathrm{ys}}\left(\in_{\mathrm{total}}\right)$ comes from independent stress–stain measurements performed on the same wires at operating conditions, like it was done in [31]; the offset yield point (or proof stress), σ_{ys0}, is taken as the stress at which 0.2% plastic deformation occurs, $\varepsilon_{\mathrm{total}}$ is the total strain which includes both the plastic, $\varepsilon_{\mathrm{pe}}$, and the elastic strain, $\varepsilon_{\mathrm{e}}=\sigma_{\mathrm{e}}/E$ and E is the Young's modulus:

$$\varepsilon_{\mathrm{total}}=\varepsilon_{\mathrm{pe}}+\varepsilon_{\mathrm{e}}. \tag{4}$$

The simulation of the transverse test follows the same loop like in the experiment. The wire is loaded and unloaded, increasing progressively the applied force. The amount of strain recovered during the unloading process is the elastic strain; the amount of strain that remains in the copper matrix and bronze components after unloading is the plastic strain. Because an elastoplastic solution is load-path dependent, the numerical model simulates the load–unload loops, as shown in figure 6. In the following simulation the maximum applied force is 30 kN.

The dynamic behavior of the system is treated as quasi-static, as the variation in time is slow compared to the natural frequencies of the system. To deal with the load–unload loops of figure 6, the model solves a sequence of intermediated problems with gradually increasing load values and uses the solutions from each previous step as initial condition for the next step (continuation method with constant predictor). At each step the total deformation gradient tensor is multiplicatively decomposed into an elastic and a plastic deformation gradient (large plastic strain assumption).

The main results of the FEM analysis are expressed in terms of Von Mises stress, plastic strain and principal strains. Depending on the material properties, when the strain exceeds the material's yield point, it may lead to plastic deformation, like in the copper and bronze domains of our 2D model, or failure, like in the Nb_3Sn domains. Failures (cracks in Nb_3Sn domains) were not implemented. In general, the invariants of the strain tensor are useful for constitutive modeling and result interpretation. For a complete discussion see [41] which, in the reversible region, describes the Nb_3Sn strain dependency. The strain function has been used in this paper to calculate the critical current density $J_{\mathrm{c}}\left(T,B,\varepsilon\right)$ at each load and unload step. The exponential strain function was developed at CERN for the axial strain dependence of Nb_3Sn and it was applied to match the critical current as measured on superconducting wires under transversal pressure in [42]. Similarly, our FEM couples the principal strain of the superconducting sub-elements obtained with the mechanical model and the scaling law describing the critical current behavior of a Nb_3Sn wire subjected to strain. This analysis tool provides useful information on how to optimize the structure of a strand to reduce the sensitivity of its critical current to transverse load.

5. Model results and discussion

In this section, we describe the FEM results for the round and rolled wires that are reported in figure 7. The plotted results are divided in a 2 by 3 matrix. The column on the left depicts the results for the round wire, while the right column lists the rolled one. The different lines report: (a) the von Mises stress distribution in the Nb_3Sn sub-elements at the maximum applied force of 30 kN, equivalent to 240 MPa of applied stress; (b) the von Mises stress distribution in the Nb_3Sn sub-elements after unload; (c) the distribution of residual plastic strain in the Cu matrix.

The first result is that the regions of the Cu matrix at higher plastic strain are also those in close proximity to the Nb_3Sn areas at higher von Mises stress both before and after unload. These areas are situated at the center of the wire and at the top and bottom corners of the hexagon formed by the Nb_3Sn sub-elements on a cross-like pattern. The plastic strain in the Cu matrix is responsible for a residual stress in the Nb_3Sn sub-elements after unload, which causes the permanent reduction of the wire critical current. This result confirms the previous assumption on the location of the high-stress regions of the wire.

The research in [21] aimed to detect cracks in round RRP® 128/127 wires after the C-WASP test using x-ray tomography combined with deep learning techniques. The investigation successfully detected longitudinal cracks positioned in the Nb_3Sn sub-elements at the wire center and in some of the corners of the hexagonal sub-element arrangement. The detected cracks were parallel to the Nb_3Sn sub-elements therefore they were not affecting the current carrying capability of the wire sample. Nevertheless, the cracks identified in [21] align closely with the sub-elements experiencing the highest stresses (>350 MPa) in our FEM, represented by the red regions in the von Mises distribution shown in figure 7(a). The Von Mises stress cannot be directly considered an indicator of the appearance of cracks in sub-elements, especially in

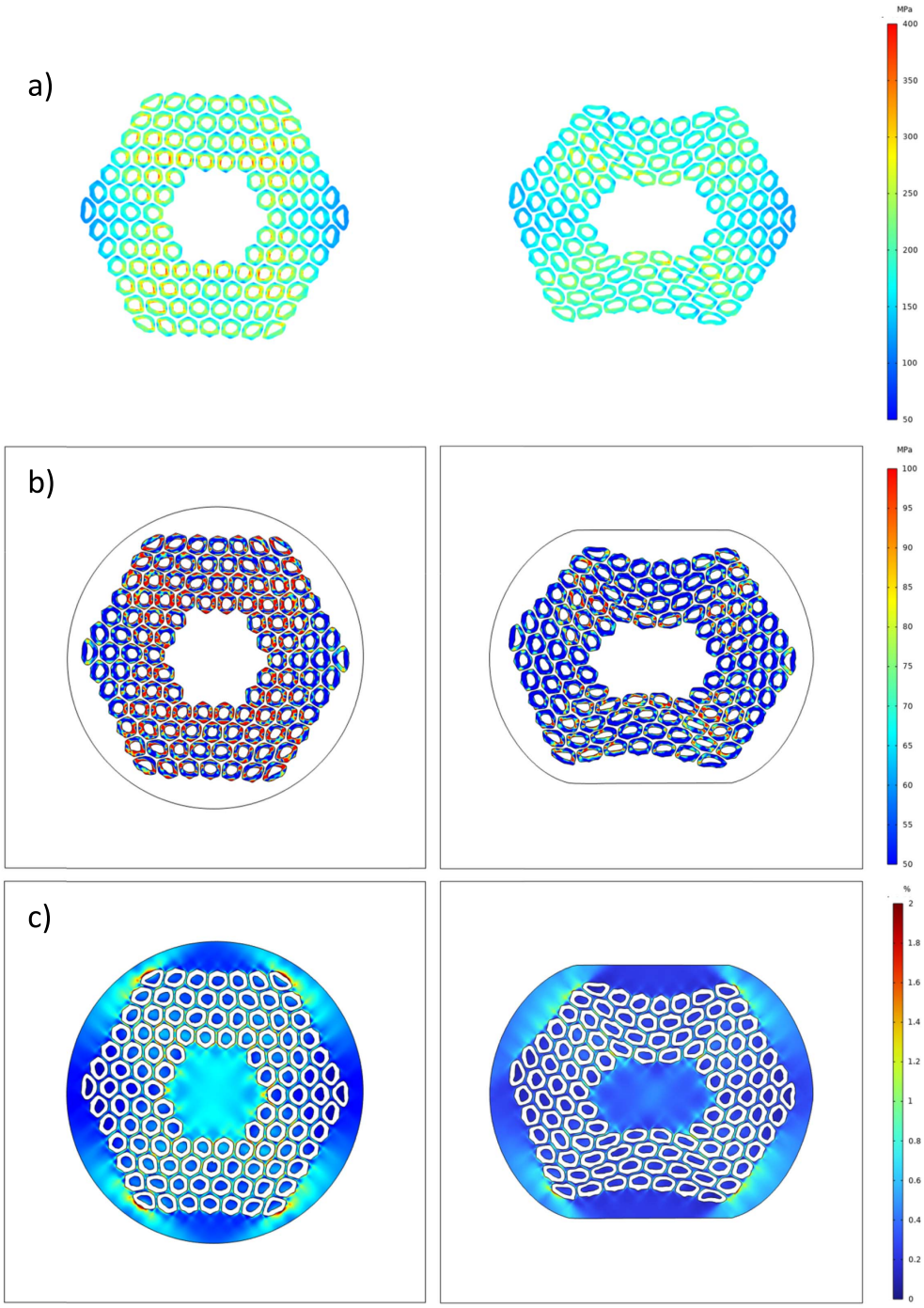

Figure 7. (a) von Mises Stress distribution in the Nb_3Sn domain at an applied load of 30 kN. (b) von Mises Stress distribution in the Nb_3Sn domain after unload from 30 kN. (c) Distribution of the residual plastic strain in the copper and bronze (sub-elements cores) domains after unload from 30 kN. In every section the plot on the left refers to the round RRP® 108/127 wire, while the right plot represents the results for the rolled wire.

brittle bodies in transverse compression; however, the similarities between the two analyses suggest that further investigations with more accurate models are necessary.

To assess the differences between the two geometries, the von Mises stress distribution, on the Nb_3Sn domains, was compared at maximum load and after unloading, as illustrated in figures 8(a) and (b), respectively. In particular, the round RRP® 108/127 wire exhibits higher stress values compared to the rolled sample. Under maximum load, a noticeable difference in average stresses is observed, with values of 185.4 MPa and 206.5 MPa for the rolled and round wires, respectively, indicating a variation of approximately 10%. Additionally, the stress levels for the rolled wire reach up to 320 MPa, while the round wire surpasses 400 MPa. After unloading,

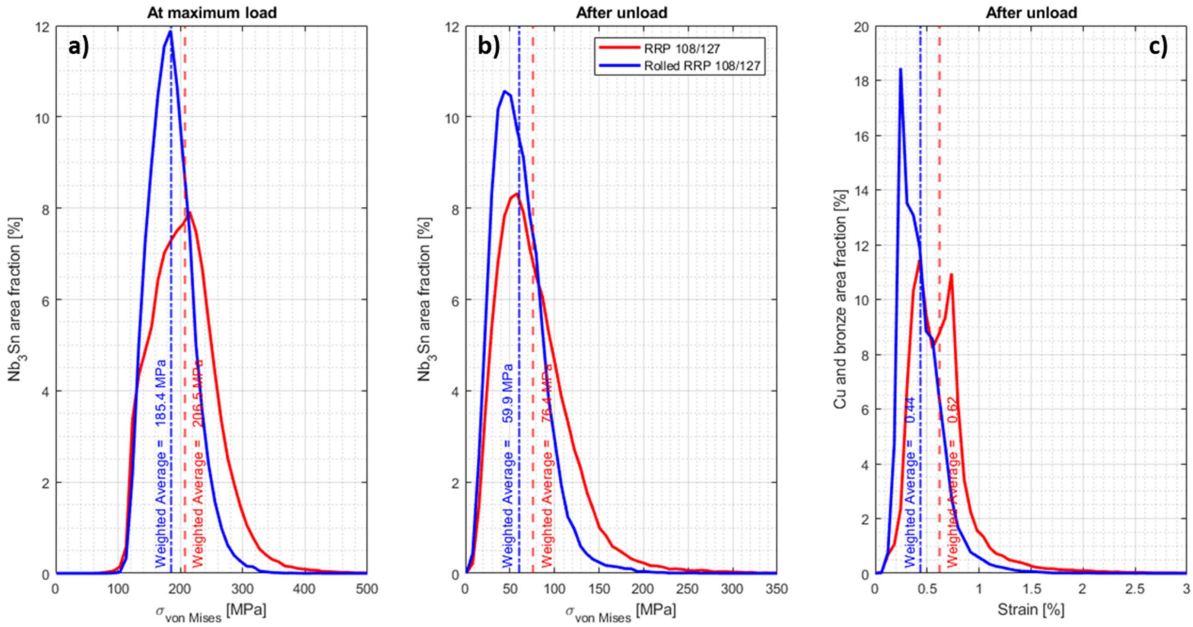

Figure 8. (a) Von Mises stress distribution in the Nb_3Sn sub-elements calculated at the maximum applied load of 30 kN; (b) Von Mises stress distribution in the Nb_3Sn sub-elements calculated after unload; (c) residual strain distribution in the Cu and bronze domains calculated after unload. The results are depicted in red for the round RRP® 108/127, while in blue for the rolled wire. The distributions are weighted on Nb_3Sn or Cu area. The vertical lines show the averages von Mises stress for the Nb_3Sn domains, and the average strain for the Cu and bronze domains.

the difference in average stress increase to about 21%, with values of 59.9 MPa and 76.4 MPa for the rolled and round samples, respectively. This distinction is visually evident in figure 7(b), where residual stresses are visibly lower in the case of the rolled wire. The residual strain distribution in the Cu and bronze domains after unloading is depicted in figure 8(c), showing that the average strain values of round and rolled wires are 0.62% and 0.44%, respectively.

Figure 9 shows the calculated I_c/I_{c0} as a function of the applied transverse stress normalized to the irreversible limit of the round wire (σ_{irr}^{round}). The reduction of I_c calculated after unloading is similar to the experimental values shown in figure 4(b). Moreover, when the round wire reaches σ_{irr}, the rolled wire still carries more than 97% of I_{c0}, yielding a result similar to that of the C-WASP test. The agreement after unloading is an indication that residual stresses in the Nb_3Sn crystal lattice caused by the plastic deformation of the Cu matrix, which are the main responsible for the critical current reduction, are well reproduced by the model.

On the other hand, the effect of the load on the critical current is more pronounced in the simulation compared to the experiment. The I_c^{load} at σ_{irr} of the round wire drops to ~60% of I_{c0}, compared to ~85% of the experiment. This significant discrepancy under load can be ascribed to the simplification adopted when conceiving the model. In order to achieve a better benchmark under load, however, it would be necessary to increase the model complexity considering the full 3D geometry, as in [20], and including the voids, or to adapt the mechanical parameters of the wire components to fit the experimental results.

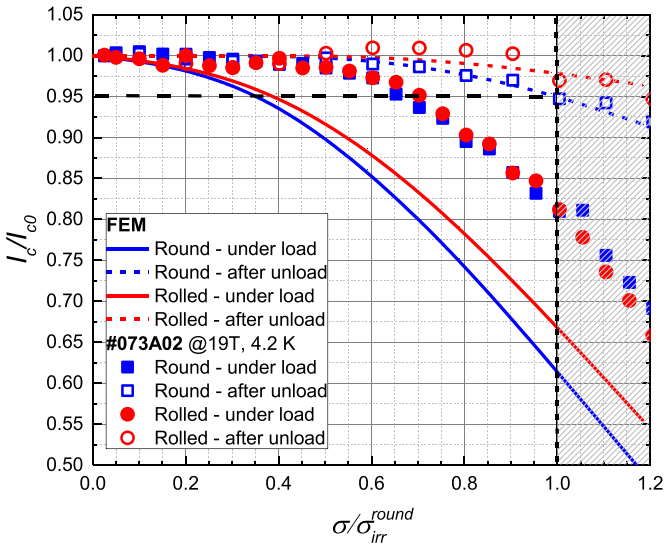

Figure 9. Dependence of the calculated I_c/I_{c0} to the $\sigma/\sigma_{irr}^{round}$ for round and rolled wires. Solid and dashed lines correspond to the results under load and after unload, respectively. Dashed black line indicates the irreversible stress limit. Solid and open symbols correspond to the experimental data under load and after unload, respectively.

Despite the simplification used, the model successfully provides valuable insights into the influence of wire geometry on stress distribution. The maximum plastic deformation occurs at the wire center and at the corners of the hexagon formed by the Nb_3Sn sub-elements, as depicted in figure 7(c).

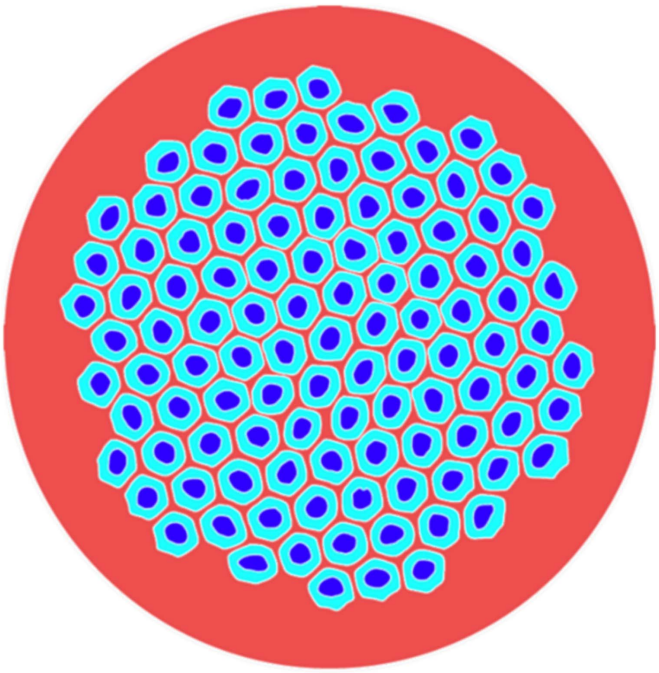

Figure 10. Geometry of the RRP® 109/127 wire design. The wire domains are shown in different color: copper matrix in red, Nb_3Sn sub-elements in cyan and bronze cores in blue.

This finding suggests that the wire geometry plays a crucial role in determining how stresses are distributed across the wire cross-section. Specifically, in the case of the 108/127 design, the plastic deformation of the bronze core leads to the accumulation of stress in the surrounding Nb_3Sn sub-elements. Furthermore, the hexagonal arrangement of the sub-elements generates an uneven distribution of the stresses with a peak in the corner sub-elements that are facing the applied load, see figure 7(a). It is worth mentioning, that the twist pitch of the wire, which is about 14 mm for this RRP® 108/127, changes the orientation of the sub-elements along the wire. For our simulations, we selected the wire cross section in the configuration that generates the highest stresses, i.e. the surface where the force is applied is perpendicular to a hexagonal side. The difference in average von Mises stress between the used configuration and the other extreme, that corresponds to the applied load facing directly a corner of the hexagonal arrangement, is less than 5%.

In the next section, based on the information collected from this analysis, we propose an alternative sub-elements distribution aimed to have a more uniform stress distribution and to increase the irreversible limit without affecting I_c.

6. RRP® 109/127: an alternative design

In this section, we propose a wire with a sub-element layout characterized by a uniform distribution of stress, both under load and after unload, across the wire cross-section. This is expected to enhance the wire irreversible limit without decreasing the wire critical current.

To achieve this, we redistributed the 108 superconducting sub-elements of the original wire, along with one additional sub-element, in a different geometry, called 109/127, which was previously tested in a UNIGE prototype internal-tin wire [43]. In this study, we selected the 109/127 sub-element distribution because the absence the Cu core is expected to reduce the residual stress in the Nb_3Sn sub-elements. The wire has a diameter of 0.7 mm, and the additional sub-element leads to a reduction of the Cu:nonCu ratio of about 2% compared to the studied RRP® 108/127. The geometry of the RRP® 109/127 wire is illustrated in figure 10.

The FEM model was used to simulate the mechanical behavior of the wire with the same steps and parameters outlined in section 4. The aim of the simulation was to evaluate the wire performance under transverse load and to investigate the impact of the change in the layout of the sub-elements on the peak stress location and residual stress distribution as well on the Cu plasticization.

The main results of the simulation, i.e. the von Mises stress distributions under an applied load of 30 kN and after unload, and the corresponding residual plastic strain in the Cu matrix, are summarized in figure 11 using the same color scale as in figure 7 to facilitate the comparison. The von Mises stress under load and after unload is distributed more homogeneously among the sub-elements in the 109/127 wire compared to the 108/127 configuration, and it is less severe compared to the original wire.

The comparison of the von Mises stress distribution on the Nb_3Sn area, at maximum load and after unload, for both wires is displayed in figures 12(a) and (b), respectively. In both cases, the von Mises stress distribution of the 108/127 layout reaches higher values compared to those of the 109/127 layout. The plot at maximum load confirms that the new design has a more homogeneous distribution than the original one. In fact, differently from the 108/127, the 109/127 has a quasi-symmetric distribution around the average value, which is reached in about ∼11% of the wire surface. The difference in the weighted average stress between the two layouts is modest, the values being 198.4 MPa and 206.5 MPa for the 109/127 and the 108/127 layouts, respectively. This corresponds to a difference of about 4%. On the other hand, the 108/127 layout has a higher wire fraction at stresses above 300 MPa. This corresponds to the numerous sub-elements showing high von Mises stress values in figure 7(a). After unload, the difference in the weighted average residual stress increases up to 15%, the values being 65.6 MPa and 76.4 MPa for the 109/127 and 108/127 layouts, respectively. This result confirms that the residual stress is higher in the 108/127 layout and, consequently, σ_{irr} is lower compared to the proposed alternative design. Interestingly, the strain distributions in the Cu and bronze domains show a similar average value in the 108/127 and 109/127 wires, i.e. 0.59% and 0.62%, see figure 12(c). Nevertheless, the two distributions are quite different; the 109/127 strain has a peak at about 0.5%, while the 108/127 wire has two peaks at about 0.4% and 0.7%.

Finally, the dependence of critical current on transverse stress for the two layouts is compared in figure 13, where the

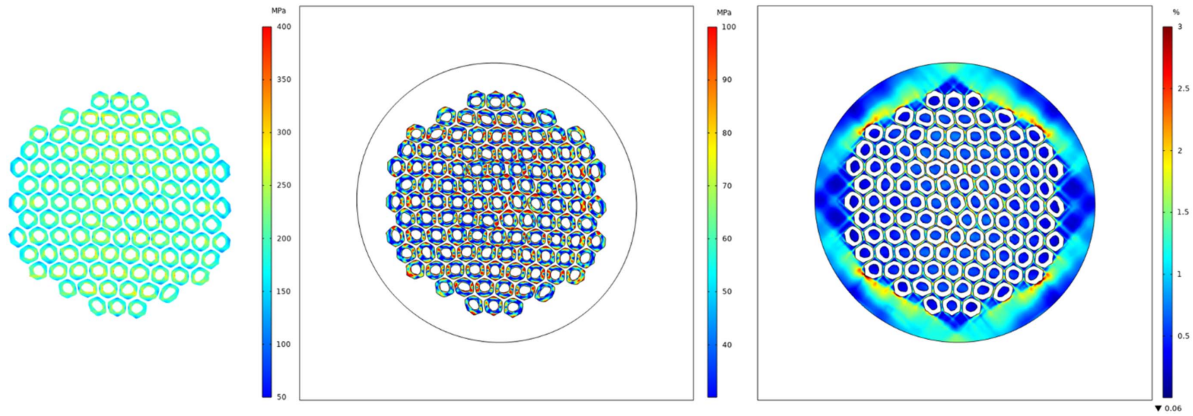

Figure 11. From left to right: von Mises Stress distribution in the Nb_3Sn domain at 30 kN applied load; von Mises Stress distribution in the Nb_3Sn domain after the unload from 30 kN; distribution of residual plastic strain in the copper domain after the unload from 30 kN. All the results referred to the 109/127 wire design.

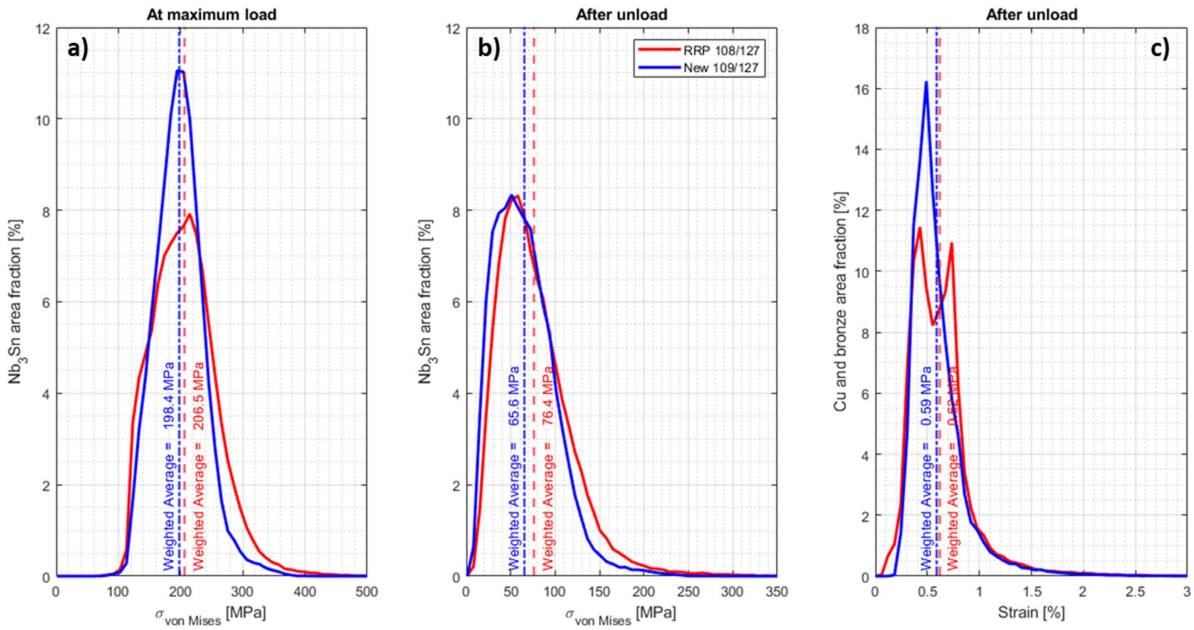

Figure 12. (a) Von Mises stress distribution in the Nb_3Sn sub-elements calculated at the maximum applied load of 30 kN; (b) Von Mises stress distribution in the Nb_3Sn sub-elements calculated after unload; (c) residual strain distribution in the Cu and bronze domains calculated after unload. The results are depicted in red for the RRP® 108/127 and in blue for the new 109/127. The distributions are weighted on Nb_3Sn or Cu area. The vertical lines show the average von Mises stress for the Nb_3Sn domains, and the average strain for the Cu and bronze domains.

I_c is normalized to the I_{c0} and plotted against the applied transverse stress normalized to the irreversible limit of the 108/127 layout (σ_{irr}^{round}). Under load, the two layouts exhibit a similar dependence. However, after unload, the two layouts exhibit different behaviors. In particular, the 109/127 layout recovers more current, reaching σ_{irr} at a stress value that is about 18% higher compared to the 108/127 layout, which is, as mentioned before, the worst orientation possible for this type of wire. This result demonstrates how σ_{irr} of a wire is influenced by the layout of its sub-elements and that it is possible to improve σ_{irr} without affecting I_c by just optimizing the distribution of the wire components.

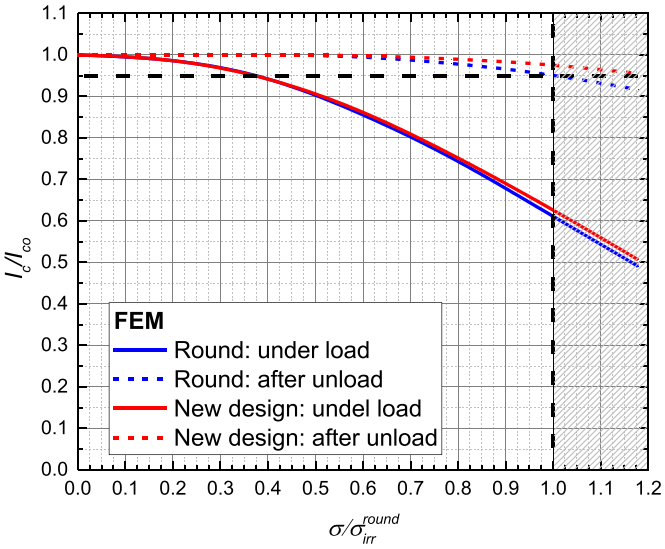

Figure 13. Dependence on the transverse stress normalized to σ_{irr}^{round} of the I_c normalized to the I_{c0} for the round 108/127 and the new 109/127 designs. Solid and dash lines correspond to the simulation results under load and after unload, respectively. Dashed black line defines the irreversible stress limits.

7. Conclusions

This study investigated the impact of rolling deformation on the transverse stress tolerance and electro-mechanical performance of high-performance Nb_3Sn wires, specifically focusing on RRP® and PIT wires. The findings shed light on the effects of rolling deformation on different wire types and provide valuable insights for the design of future high-field magnets, based on Rutherford cables, in particle accelerators.

PIT wires exhibited a reduction in I_{c0} of approximately 9% due to rolling deformation, primarily caused by deformations in the Nb-alloy filaments that affect Nb_3Sn formation. However, the critical current behavior of both round and rolled wires was comparable above 70 MPa, likely due to the transverse load primarily affecting the filaments at the wire core. The difference in critical currents between rolled and round wires decreased upon unloading from increasing applied stresses, ranging from 3% to 6% above 100 MPa. Notably, rolling deformation did not significantly affect the irreversible limit (σ_{irr}) of PIT wires when considering the I_{c0} of the round wire as reference. The σ_{irr} of the round and rolled PIT wires was found to be about 110 MPa.

Rolling deformation did not result in any degradation of I_{c0} in the 108/127 RRP® wire. In fact, a slight increase in I_{c0} (approximately 4%) was observed, possibly due to variations within the wire billet or differences in the initial strain state of the wire during sample mounting. Both round and rolled RRP® wire samples exhibited similar behavior under load. However, the rolled RRP® wire demonstrated a higher σ_{irr}, 185 MPa, compared to the round wire, 160 MPa, (approximately 15% higher) suggesting that rolling deformation did not harm and even enhanced the stress tolerance of RRP® wires.

A 2D-mechanical FEM model was used to investigate the stress distribution within the Nb_3Sn sub-elements and the plastic deformation of the copper matrix in the RRP® wire. The model confirmed the negative influence of residual stress generated by the copper matrix on the Nb_3Sn sub-elements, which is the primary cause of critical current degradation in RRP® wires. The model highlighted the detrimental effects of the copper core and of the hexagonal distribution of the sub-elements on the wire behavior. Additionally, the model predicted lower stresses and a higher σ_{irr} (~20%) in rolled RRP® wires, further supporting the experimental results.

Based on the model insights, an alternative sub-element layout (109/127) for RRP® wires was proposed to mitigate the impact of the copper core on the wire performance. This new design showed a more homogeneous von Mises stress distribution and lower peak stresses. Simulations demonstrated that the irreversible stress limit of the 109/127 layout was approximately 18% higher than that of the 108/127 layout, while the critical current behavior remained unaffected under load. This result offers insights into wire design considerations and potential improvements, particularly highlighting the benefits of the alternative sub-element layout, e.g. 109/127, in enhancing stress tolerance while maintaining the wire current-carrying properties.

Data availability statement

The data that support the findings of this study are available upon reasonable request from the authors.

Acknowledgments

This work was done under the auspices of CHART (Swiss Accelerator Research and Technology Collaboration, https://chart.ch).

Financial support was provided by the Swiss National Science Foundation (Grant No. 200021_184940) and by the European Organization for Nuclear Research (CERN), Memorandum of Understanding for the FCC Study, Addendum FCC-GOV-CC-0176 (KE4612/ATS).

The authors are also grateful to Damien Zurmuehle for all his help with the laboratory work and the experiments.

ORCID iDs

T Bagni https://orcid.org/0000-0001-8654-783X
C Calzolaio https://orcid.org/0000-0002-7164-7288
G Bovone https://orcid.org/0000-0002-9161-7828
J Ferradas-Troitino https://orcid.org/0000-0001-7874-9722
C Senatore https://orcid.org/0000-0002-9191-5016

References

[1] Bottura L and Rossi L 2016 Magnets for particle accelerators and colliders *Digital Encyclopedia of Applied Physics* (Wiley) pp 1–40

[2] Apollinari G *et al* 2015 *High-Luminosity Large Hadron Collider (HL-LHC): Preliminary Design Report* (CERN) p. Medium: ED; Size p 19

[3] Abada A *et al* 2019 FCC-hh: the hadron collider *Eur. Phys. J. Spec. Top.* **228** 755–1107

[4] Foner S and McNiff E J 1981 Upper critical fields of cubic and tetragonal single crystal and polycrystalline Nb_3Sn in DC fields to 30 tesla *Solid State Commun.* **39** 959–64

[5] Matthias B T, Geballe T H, Geller S and Corenzwit E 1954 Superconductivity of Nb_3Sn *Phys. Rev.* **95** 1435

[6] Mitchell N and Devred A 2017 The ITER magnet system: configuration and construction status *Fusion Eng. Des.* **123** 17–25

[7] Polyanskii A A, Lee P J, Jewell M C, Barzi E, Turrioni D, Zlobin A V and Larbalestier D C 2009 Evidence for highly localized damage in internal tin and powder-in-tube Nb_3Sn strands rolled before reaction obtained from coupled magneto-optical imaging and confocal laser scanning microscopy *Supercond. Sci. Technol.* **22** 095008

[8] Brown M, Tarantini C, Starch W, Oates W, Lee P J and Larbalestier D C 2016 Correlation of filament distortion and RRR degradation in drawn and rolled PIT and RRP Nb_3Sn wires *Supercond. Sci. Technol.* **29** 084008

[9] Sorbi M, Bellomo G, Caiffi B, Fabbricatore P, Farinon S, Marinozzi V and Volpini G 2017 The EuroCirCol 16T cosine–theta dipole option for the FCC *IEEE Trans. Appl. Supercond.* **27** 1–5

[10] Felice H *et al* 2019 F2D2: a block-coil short-model dipole toward FCC *IEEE Trans. Appl. Supercond.* **29** 1–7

[11] Toral F, Garcia-Tabares L, Martinez T, Munilla J, Ruuskanen J, Salmi T and Stenvall A 2017 EuroCirCol 16 T common-coil dipole option for the FCC *IEEE Trans. Appl. Supercond.* **27** 1–5

[12] Caspi S *et al* 2015 Design of an 18-T canted cosine–theta superconducting dipole magnet *IEEE Trans. Appl. Supercond.* **25** 1–5

[13] Valente R, Bellomo G, Caiffi B, Fabbricatore P, Farinon S, Mariotto S, Pampaloni A, Ricci A M, Sorbi M and Statera M 2019 Baseline design of a 16 T cos theta bending dipole for the future circular collider *IEEE Trans. Appl. Supercond.* **29** 1–5

[14] Ebermann P *et al* 2018 Irreversible degradation of Nb_3Sn Rutherford cables due to transverse compressive stress at room temperature *Supercond. Sci. Technol.* **31** 065009

[15] Puthran K, Barth C, Ballarino A, Devred A and Arndt T 2023 Onset of mechanical degradation due to transverse compressive stress in Nb_3Sn rutherford-type cables *IEEE Trans. Appl. Supercond.* **33** 1–6

[16] De Marzi G, Bordini B and Baffari D 2021 On the mechanisms governing the critical current reduction in Nb_3Sn Rutherford cables under transverse stress *Sci. Rep.* **11** 7369

[17] Ekin J W 1987 Effect of transverse compressive stress on the critical current and upper critical field of Nb_3Sn *J. Appl. Phys.* **62** 4829–34

[18] Haken B T, Godeke A and Kate H H J T 1999 The strain dependence of the critical properties of Nb_3Sn conductors *J. Appl. Phys.* **85** 3247–53

[19] Troitino J F, Bagni T, Barth C, Bordini B, Ferracin P, Gamperle L, Tommasini D, Zurmuehle D and Senatore C 2021 Effects of the initial axial strain state on the response to transverse stress of high-performance RRP Nb_3Sn wires *Supercond. Sci. Technol.* **34** 035008

[20] Baffari D and Bordini B 2022 Effect of the sub-elements layout on the electro-mechanical properties of high Jc Nb_3Sn wires under transverse load: numerical simulations *IEEE Trans. Appl. Supercond.* **32** 1

[21] Bagni T, Mauro D, Majkut M, Rack A and Senatore C 2022 Formation and propagation of cracks in RRP Nb_3Sn wires studied by deep learning applied to x-ray tomography *Supercond. Sci. Technol.* **35** 104003

[22] Senatore C, Bagni T, Ferradas-Troitino J, Bordini B and Ballarino A 2023 Degradation of Ic due to residual stress in high-performance Nb_3Sn wires submitted to compressive transverse force *Supercond. Sci. Technol.* **36** 075001

[23] Gämperle L, Ferradas J, Barth C, Bordini B, Tommasini D and Senatore C 2020 Determination of the electromechanical limits of high-performance Nb_3Sn Rutherford cables under transverse stress from a single-wire experiment *Phys. Rev. Res.* **2** 013211

[24] Bordini B, Bottura L, Mondonico G, Oberli L, Richter D, Seeber B, Senatore C, Takala E and Valentinis D 2012 Extensive characterization of the 1 mm PIT Nb_3Sn strand for the 13-T FRESCA2 magnet *IEEE Trans. Appl. Supercond.* **22** 6000304

[25] Mondonico G, Seeber B, Ferreira A, Bordini B, Oberli L, Bottura L, Ballarino A, Flükiger R and Senatore C 2012 Effect of quasi-hydrostatical radial pressure onIcof Nb_3Sn wires *Supercond. Sci. Technol.* **25** 115002

[26] Fleiter J *et al* 2017 Optimization of Nb_3Sn Rutherford cables geometry for the high-luminosity LHC *IEEE Trans. Appl. Supercond.* **27** 1–5

[27] Bagni T, Bovone G, Rack A, Mauro D, Barth C, Matera D, Buta F and Senatore C 2021 Machine learning applied to x-ray tomography as a new tool to analyze the voids in RRP Nb_3Sn wires *Sci. Rep.* **11** 7767

[28] Bagni T, Haldi H, Mauro D and Senatore C 2022 Tomography analysis tool: an application for image analysis based on unsupervised machine learning *IOP SciNotes* **3** 015201

[29] Meyer M Mechanical characterization of CTD 101K and Stycast 2850 FT epoxy resin systems. 2018, CERN (available at: https://edms.cern.ch/ui/#!master/navigator/document?D:100044996:100044996:subDocs)

[30] Ferradas Troitino J 2018 Impregnated epoxy—flexural tests (CERN) (available at: https://edms.cern.ch/ui/#!master/navigator/document?D:100059980:100059980:subDocs)

[31] Calzolaio C, Mondonico G, Ballarino A, Bordini B, Bottura L, Oberli L and Senatore C 2015 Electro-mechanical properties of PIT Nb_3Sn wires under transverse stress: experimental results and FEM analysis *Supercond. Sci. Technol.* **28** 055014

[32] Seeber B, Ferreira A, Abacherli V, Boutboul T, Oberli L and Flukiger R 2007 Transport properties up to 1000 A of Nb *Nb_3Sn* wires under transverse compressive stress *IEEE Trans. Appl. Supercond.* **17** 2643–6

[33] Segal C *et al* 2016 Evaluation of critical current density and residual resistance ratio limits in powder in tube Nb_3Sn conductors *Supercond. Sci. Technol.* **29** 085003

[34] Sanabria C, Field M, Lee P J, Miao H, Parrell J and Larbalestier D C 2018 Controlling Cu–Sn mixing so as to enable higher critical current densities in RRP®Nb3Sn wires *Supercond. Sci. Technol.* **31** 064001

[35] Scheuerlein C *et al* 2014 Stress distribution and lattice distortions in Nb_3Sn multifilament wires under uniaxial tensile loading at 4.2 K *Supercond. Sci. Technol.* **27** 044021

[36] Haibel A and Scheuerlein C 2007 Synchrotron tomography for the study of void formation in internal tin *Nb_3Sn* superconductors *IEEE Trans. Appl. Supercond.* **17** 34–39

[37] Scheuerlein C, Di Michiel M and Haibel A 2007 On the formation of voids in internal tin Nb_3Sn superconductors *Appl. Phys. Lett.* **90** 132510

[38] Barth C, Seeber B, Rack A, Calzolaio C, Zhai Y, Matera D and Senatore C 2018 Quantitative correlation between the void morphology of niobium-tin wires and their irreversible

critical current degradation upon mechanical loading *Sci. Rep.* **8** 6589
[39] Mitchell N 2005 Finite element simulations of elasto-plastic processes in Nb_3Sn strands *Cryogenics* **45** 501–15
[40] Structural Mechanics Module User's Guide 2018 *Comsol Multiphysics®, version 5.4*
[41] Bordini B, Alknes P, Bottura L, Rossi L and Valentinis D 2013 An exponential scaling law for the strain dependence of the Nb_3Sn critical current density *Supercond. Sci. Technol.* **26** 075014
[42] Wang T, Chiesa L, Takayasu M and Bordini B 2014 A novel modeling to predict the critical current behavior of Nb_3Sn PIT strand under transverse load based on a scaling law and finite element analysis *Cryogenics* **63** 275–81
[43] Buta F *et al* 2018 Towards a Nb_3Sn conductor for FCC *FCC Week*